Spatial variability and non-linearity of strong ground motion near a fault

H. Karabulut, Michel Bouchon

Spatial variability and non-linearity of strong ground motion near a fault

Hayrullah Karabulut[1] and Michel Bouchon[2]

[1]*Boğaziçi University, Istanbul, Turkey. E-mail: kara@boun.edu.tr*
[2]*Université Joseph Fourier,* BP 53, 38041 *Grenoble, France*

SUMMARY

We present observations of ground accelerations recorded at a small array close to the fault during the Düzce earthquake and its early aftershocks. The records show the strong spatial variability of ground acceleration over distances of only a few hundred metres. During the main shock, the peak horizontal acceleration values ranged from 0.3 to about 1.0 g at stations distant of 1.5 km only. We attribute this spatial variability to a fault zone site effect as peak ground acceleration steadily increases as the distance to the fault trace decreases. The spectral ratio between the ground motion recorded near the fault and the one outside the fault zone shows a shift of the spectral peak to lower frequencies with increasing peak accelerations. Such an observation suggests a non-linear behaviour of the fault zone due to the strong ground shaking. As much as a 45 per cent reduction in the shear wave velocity is necessary for the observed shifts. The opening of pre-existing cracks throughout the fault zone is the proposed mechanism to account for the observed shear wave reductions. The observation that elastic fault zone properties are soon recovered following episodes of large strains shows that cracks and fissures close rapidly after the strong shaking is over.

Key words: fault zone, nonlinear, strong motion, trapped waves.

GJI Seismology

INTRODUCTION

Although the non-linear elastic response of soils under large strains has long been known and investigated, seismologists have remained sceptical on the extent of non-linearity during earthquakes due to lack of evidence from strong motion observations. However, with the increasing availability of strong motion data over the last decade, many examples of non-linearity have been observed during large earthquakes. While a number of studies has provided evidence of non-linearity in shallow stiff-soil sites (Beresnev & Wen 1996; Field *et al.* 1998; Pavlenko & Irikura 2002), indications that non-linearity may also occur in the vicinity of faults come from observations that large earthquakes can create coseismic reductions in seismic wave velocities at near fault locations in presence of unconsolidated sedimentary rocks (Dodge & Beroza 1997). Time dependent measurements in the fault zones (FZ) have also revealed that the healing of a fault following an earthquake can be interrupted by the strong motion created by a nearby earthquake (Vidale & Li 2003; Rubinstein & Beroza 2004; Peng & Ben-Zion 2005, 2006).

In studies of non-linear elasticity of many rocks, this type of behaviour was observed at strains $\sim10^{-6}$ which resulted in a persistent drop in elastic modulus and increase in material damping. After the stress is removed, the material properties recover towards their original values as the logarithm of elapsed time. An important feature of this effect, which is called *slow dynamics,* is that the elastic modulus decreases in response to symmetric stress cycling of either sign,

thus violating the symmetry of the inducing source (TenCate *et al.* 2000).

The FZ may have significantly different behaviour during strong ground motion from the soft-soil sites. The FZ are narrow, heterogenous and fractured zones embedded in relatively persistent materials with different elastic properties (e.g. Ben-Zion 1998). These zones may have thicknesses of several tens of metres to several hundreds of metres at the surface (Li *et al* 1994, 1998, 2000) and are relatively narrower at depth. Because of their nature, they are associated with lower seismic velocities than the surrounding rocks and thus form low velocity channels which may trap seismic energy. The seismic waves propagating through the low velocity FZ display specific wave propagation effects such as head waves, trapped waves, anisotropy, scattering and attenuation. Several observational studies have provided evidence of these fault zone related effects. Detailed descriptions of the properties of the fault zone waves are given by Cormier & Spudich (1984), Ben-Zion & Aki (1990), Ben-Zion (1998), Rovelli *et al.* (2002), Peng *et al*. (2003) and McGuire & Ben-Zion (2005). Leary *et al.* (1987), Igel *et al.* (1997, 2002), Fohrmann *et al.* (2001, 2004) and Jahnke *et al.* (2002) have discussed properties of guided waves in irregular 2- and 3-D FZ structures.

Fault zone related effects on seismic waves have been clearly observed on a few continental faults. Although most of these investigations have been carried out on branches of the San Andreas fault, the earthquakes in the Marmara region of northwestern Turkey of 1999 August 17 and 1999 November 12, have also provided a good

environment for studying the properties of FZ. A tomographic study crossing the NAF near the Izmit rupture zone revealed low velocity fault zone correlated with the seismicity (Karabulut *et al*. 2003). Ben-Zion *et al*. (2003) analysed a large seismic data set recorded 6 months after the 1999 $M_w = 7.4$ Izmit earthquake by a local PASSCAL network on the Karadere-Düzce branch of the North Anatolian Fault (NAF). They observed large amplifications at sites within tens of metres from the surface expression of the rupture with respect to the off-fault stations. Their traveltime and waveform analysis showed that the depth extent of the structure in the fault zone producing trapped waves is 3–4 km. Shear wave splitting measurements on the Karadere-Düzce branch of NAF by Peng & Ben-Zion (2004) show an anisotropy confined to the upper 3–4 km from which they estimate a crack density of 7 per cent. Peng & Ben-Zion (2006) analysed temporal variations of seismic velocity along this segment of the NAF using seismograms generated by repeating earthquake clusters in the aftershock zones of the Izmit and Düzce earthquakes. They observed clear step-like delays in the direct *S* and early *S*-coda waves (sharp seismic velocity reduction) immediately after the Düzce main shock, followed by gradual logarithmic-type recoveries.

In the present study we use data recorded at a small array near the fault during the $M_w = 7.2$ Düzce earthquake and its early aftershocks to investigate the spatial variability of strong ground motion near the fault during a devastating earthquake and to determine the extent of non-linearity.

THE EXPERIMENT

On 1999 November 12, a few hours before the Düzce earthquake, we installed an array of seismic stations near the eastern termination of the Izmit rupture, along the Karadere fault segment which forms with the Düzce fault the Eastern section of the northern strand of the NAF System (Fig. 1). The Düzce fault along which 1999 November 12 earthquake occurred is approximately 45 km long. On its western termination the alluviums of the Düzce plain and the rocks forming the Almacık mountain are in contact, whereas on the eastern termination the fault is observed in the basement rocks (Fig. 2). The NE–SW trending, 40-km-long Karadere fault runs between the Eocene, Plio-Quaternary rock units on the north and suture zone rocks forming the Almacık Block (Herece & Akay 2003).

The array consisted of four six-channel seismic stations with both weak and strong motion sensors. They were located along the fault, at a spacing of a few hundred metres (Table 1). The array was deployed in view of the unusually high local seismic activity that we had observed during the previous 2 d in the area (Bouchon & Karabulut 2002) and was meant to investigate its origin. The array location, shown in Fig. 1, is between the villages of Karadere and Gölyaka and lies about 6 km away from the western extremity of the surface break of the Düzce earthquake and about 9 km from the Eften Lake area where the Düzce slip reached over 4 m (Akyuz *et al*. 2002; Bouin *et al*. 2004). The region is hilly with little sedimentary cover and many hard rock outcrops. The station furthest
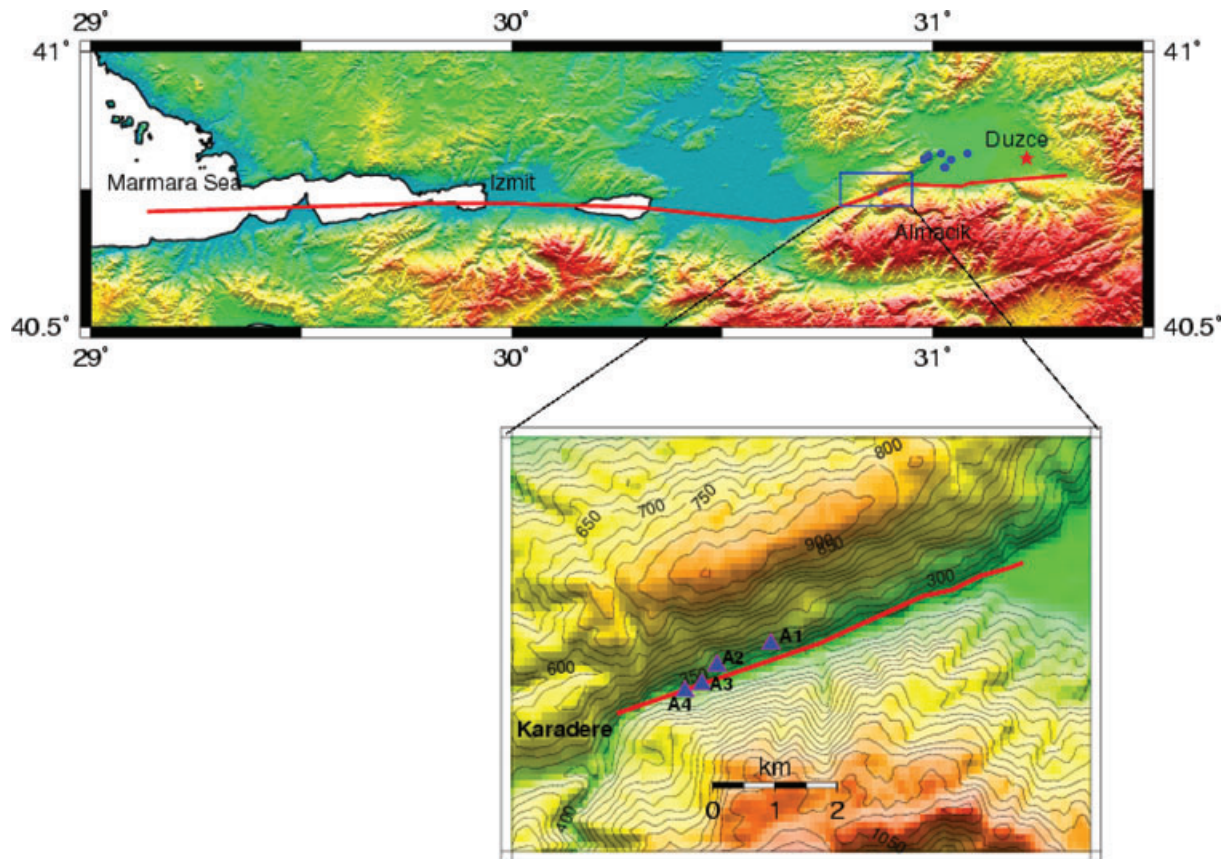
Figure 1. Location of the array with respect to the North Anatolian Fault segment which ruptured during the Izmit and Düzce earthquakes (solid line). The triangles show the location of the four stations. The epicentre of the Düzce earthquake is indicated by a star. The aftershocks used in the study are shown by blue circles (Özalaybey *et al*. 2000).
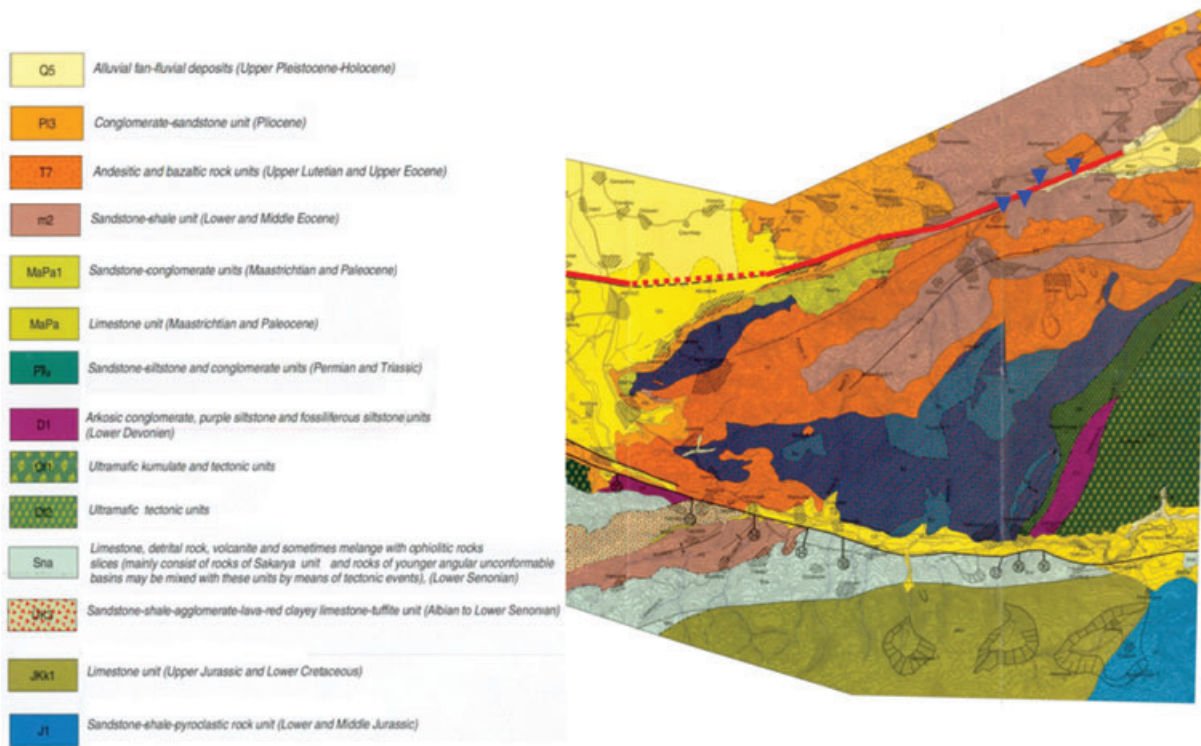
Figure 2. Geology map of the study area. The fault is indicated by red line. The stations are indicated by blue triangles (Modified from Herece & Akay 2003).

Table 1. Coordinates of the stations in the array and distances from the epicentre of the Düzce main shock and to the surface fault trace.

Station	Latitude	Longitude	Epicentral distance (km)	Interstation distance (m)	Distance to the fault trace (m)
A1	40.7489	30.8892	22.85	0	150
A2	40.7458	30.8790	23.78	930	50
A3	40.7431	30.8761	24.12	1280	20
A4	40.7421	30.8729	24.39	1550	1

from the fault (A1) lies about 150 m from the surface fault break. Other stations were located at about 50 m (A2), 20 m (A3) and 1 m (A4) from the surface fault trace. All sensors were installed near the ground surface, buried below the top soil, on the sandstone unit (Fig. 2).

The recording of the main shock and of the early aftershocks by a closely spaced array provides an opportunity to investigate the spatial variability of strong ground motion near a fault.

## HIGH SPATIAL VARIABILITY OF GROUND ACCELERATIONS

The main shock accelerations were recorded at three stations, the fourth strong-motion recording not having triggered properly during the earthquake. The accelerations at the two sites located at the extremities of the linear array, A1 to the east and A4 to the west, are shown in Fig. 3. Although the two stations were only 1.5 km apart, (with A1 closer to the epicentre), the ground accelerations there during the earthquake were strikingly different, reaching levels of 0.30 g at one site and about 1.0 g at the other one. The accelerometers that we used were set to record acceleration levels of up to 0.75 g. At station A4, this level was exceeded by five of the peaks on the N–S component and by one of the peak on the E–W component. We interpolated the missing values by cubic spline interpolation

(Appendix A). Peak acceleration at the third recording station, A2, was 0.40 g.

The corresponding ground velocities are displayed in Fig. 4. They show that, although the two sites, A1 and A4, underwent widely different acceleration time-histories during the earthquake, they had comparable ground velocity histories, with peak values around 40 cm s^{-1}. It is worthwhile to mention that the interpolation of the clipped peaks did not create any transients after integration.

The acceleration spectra of the N–S components at the three recording sites are displayed in Fig. 5. Up to 2.5 Hz, ground motion is almost the same at the three locations. The large amplification at A4 occurs between 3 and 8 Hz, with a peak around 4 Hz.

Twenty minutes after the main shock, a peak acceleration of about 1.0 g was reached again at A4 (Fig. 6). Accelerograms recorded at the other stations yield peak accelerations of 0.23 g (A1), 0.33 g (A2) and 0.68 g (A3), demonstrating a great spatial variability over interstation distances of only a few hundred metres. As the only objective parameter differentiating the closely spaced stations is their distance to the surface trace of the fault, we interpret the regular increase of peak ground acceleration with decreasing distance to the fault as a site effect of the fault zone. This pattern stayed unchanged for all the aftershocks analysed. For instance, within an hour of the main shock, peak accelerations of 0.75 and 0.60 g were reached again at A4, while the corresponding peak accelerations at A1 were 0.30 and 0.14 g, respectively.
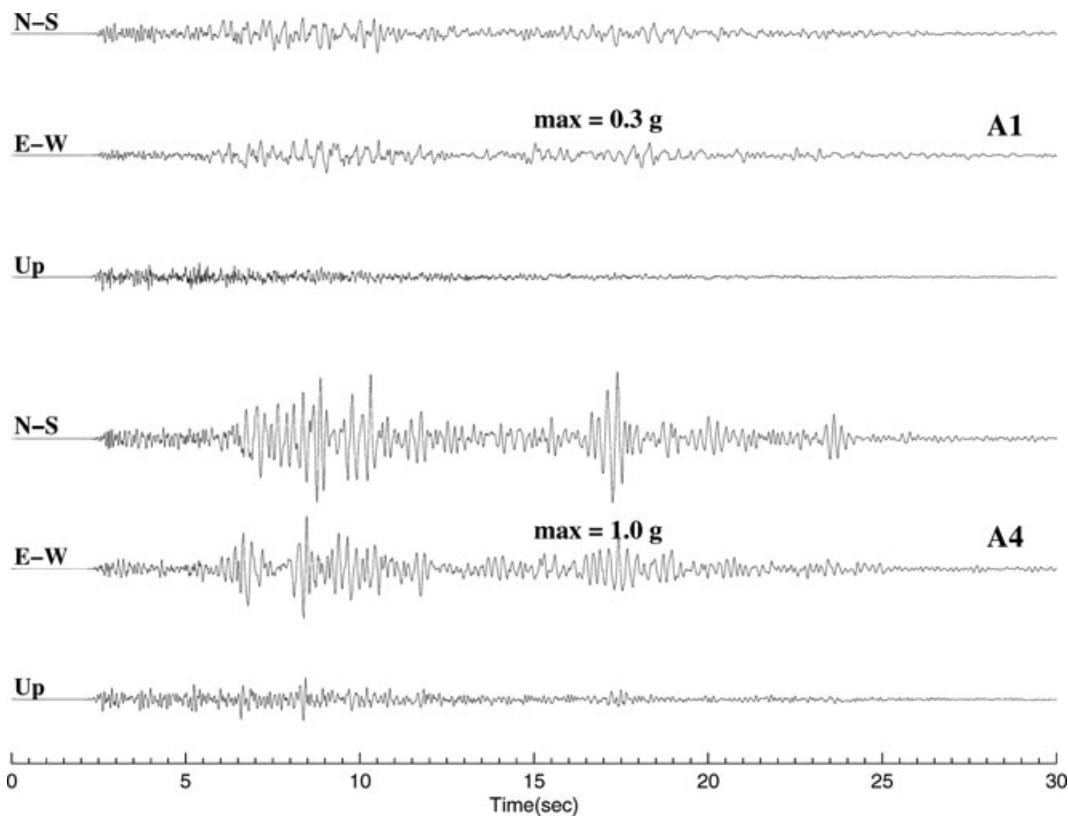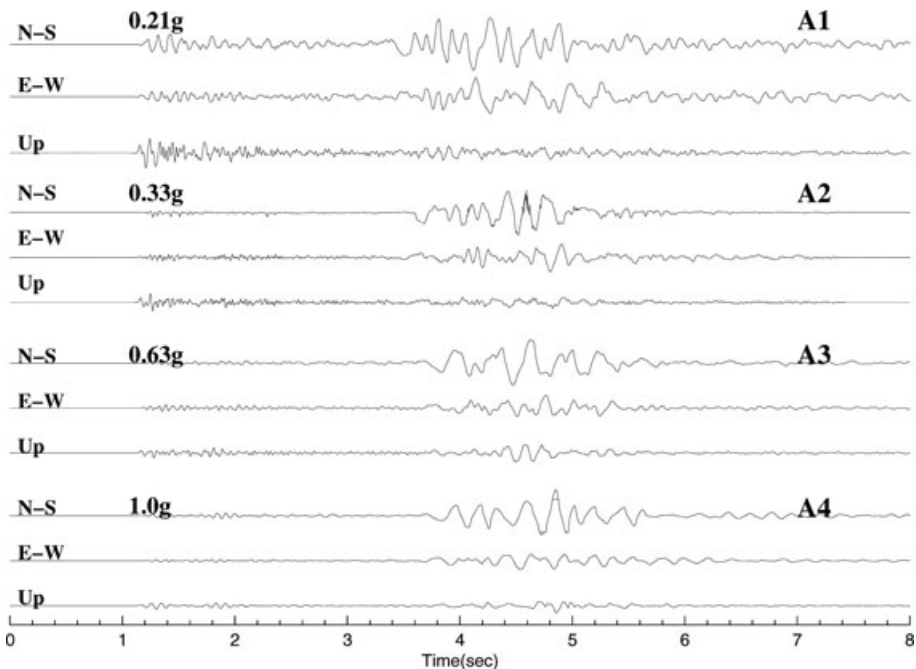
Figure 3. Ground accelerations recorded during the main shock at two stations, 1.5 km apart. The amplitude scale is the same for all traces. Peaks above 0.75 g have been reconstructed by Spline interpolation.
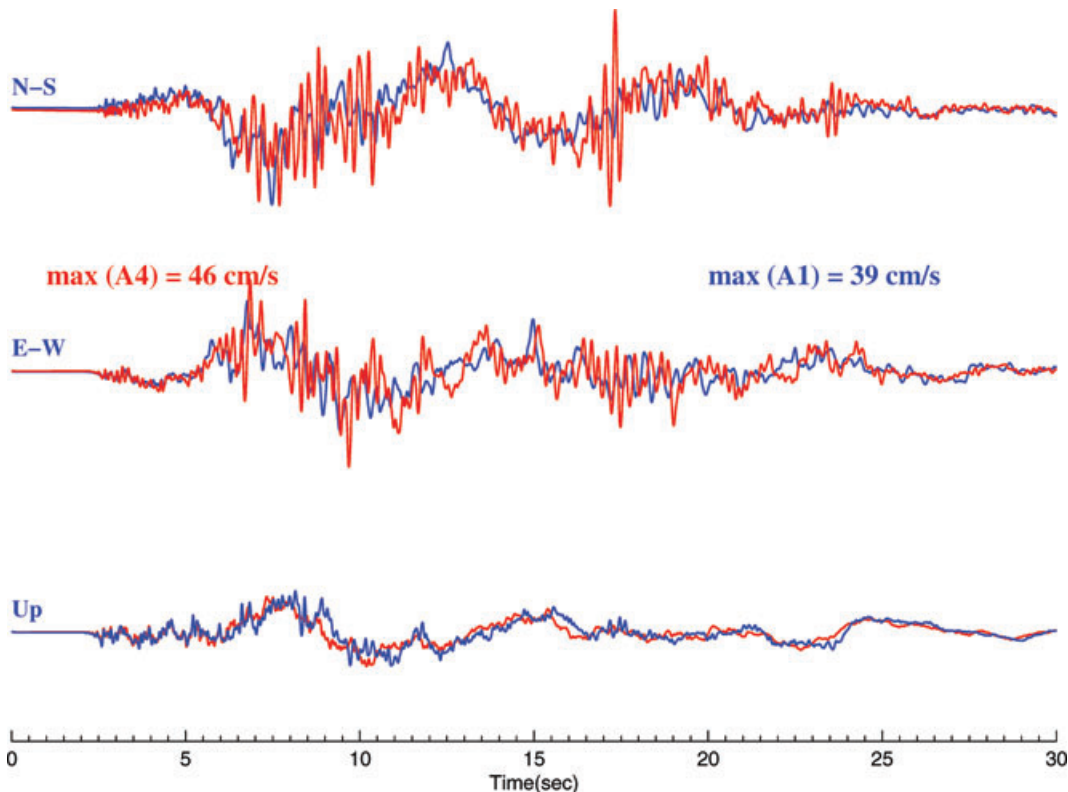
Figure 4. Ground velocities obtained by integration of the acceleration records of Fig. 2. The amplitude scale is the same for all traces.
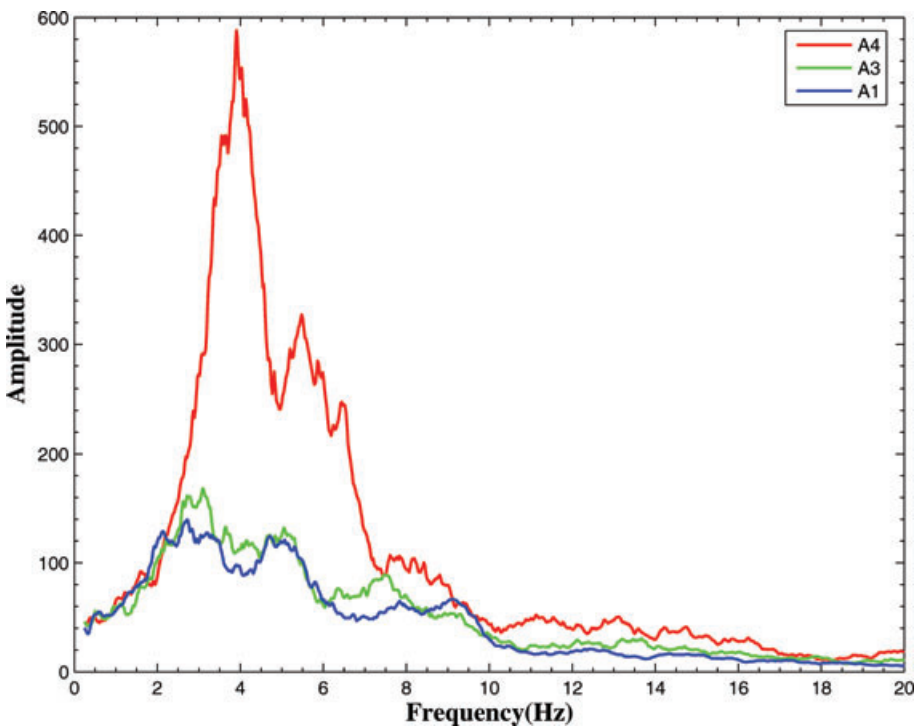
Figure 5. Acceleration spectra at the three stations of the array which recorded the main shock.

Figure 6. Ground accelerations recorded during the strongest-felt aftershock at the four stations of the array, 20 min after the main shock. Peak acceleration values at each station are indicated. The clipped acceleration values at 0.75 g of the N–S component at A4 are indicated by the flat line.

In order to investigate whether weaker shaking still exhibits this high degree of spatial variability, we present in Fig. 7 the time-histories of horizontal ground accelerations over the 4 min following the main shock at A1 and A4. The 'noise' level on these records is close to 0.01 g and represents the level of nearly constant shaking of the ground in the minutes following the earthquake. The comparison between the two sites shows an amplification of the horizontal ground acceleration at A4, by an average factor of 2.2.

After the Düzce earthquake, Ben-Zion *et al.* (2003) carried out specific experiments along the Karadere segment of the NAF, the zone of our recordings, to investigate the characteristics of the fault zone. From the recordings of waves trapped in the fault zone, they were able to infer the width of the fault zone to be about 100 m. Such a width, which as we will show later is confirmed by our observations, places station A1 outside the fault zone, A2 near the edge of the fault zone, and A3 about half-way inside the fault zone,
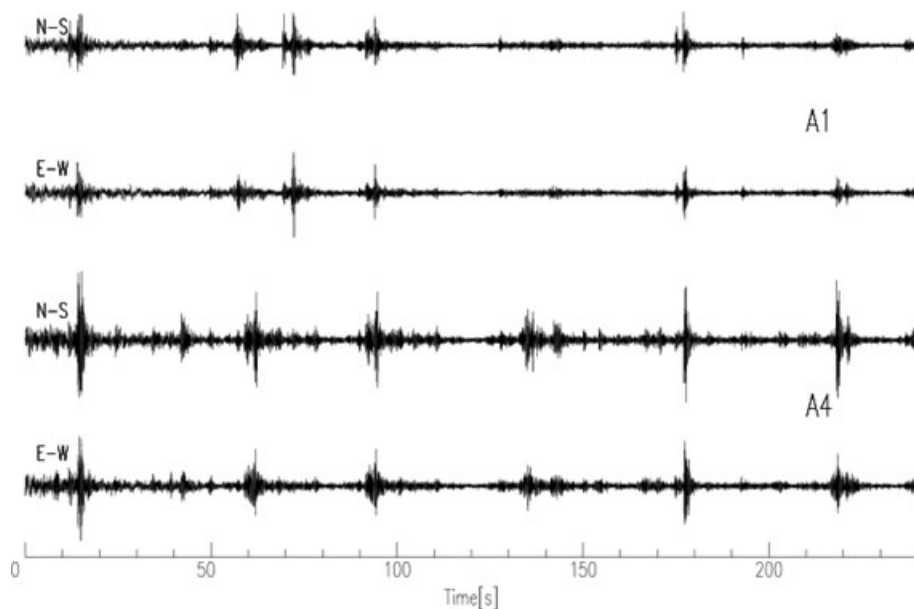
Figure 7. Recordings of horizontal ground accelerations over the 4 min following the main shock at two stations of the array, 1.5 km apart. The amplitude scale is the same for all traces. The maximum acceleration level over this time period is 0.06 g.

while A4 lies in the middle of the fault zone. Thus, combining inferred fault zone geometry from Ben-Zion *et al*. (2003) with our strong motion recordings, we infer that the high spatial variability of ground acceleration that we observe is a fault zone site effect. The resulting amplification of peak ground acceleration (PGA) near the fault relative to its value outside the fault zone lies in the range 2.5–4 for the main shock and the strongest-felt aftershocks.

FREQUENCY SHIFT OF PEAK AMPLIFICATION WITH ACCELERATION LEVEL

The horizontal spectral ratios between the station located near the fault (A4) and the one outside the fault zone (A1) for the main shock and the strongest-felt aftershocks are displayed in Figs 8 and 9,
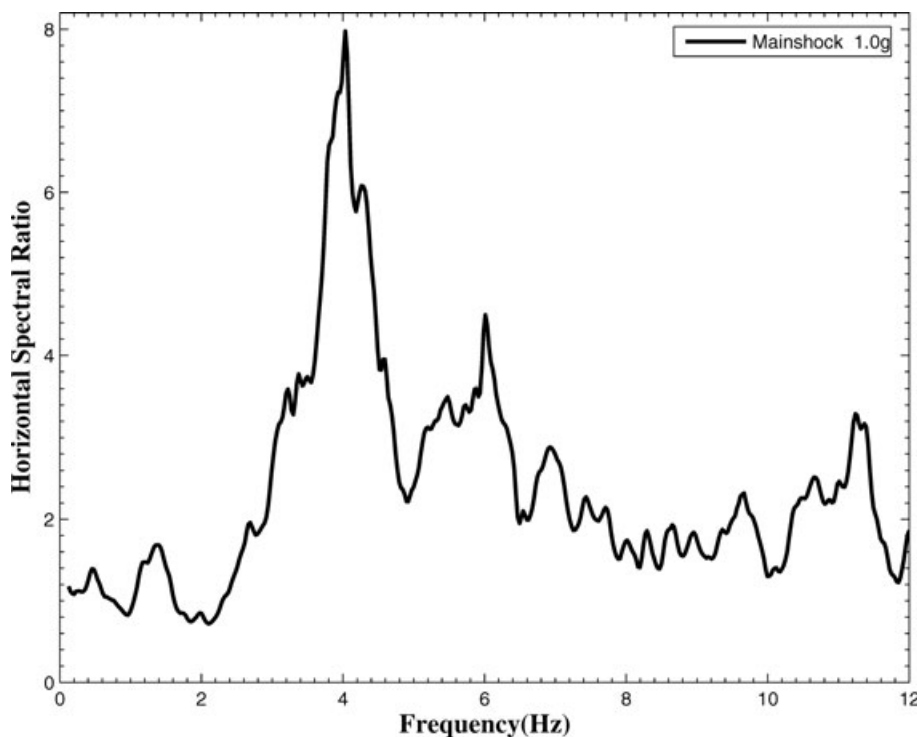
Figure 8. Horizontal spectral ratios between the two farthest stations of the array A4 and A1 for the main shock.
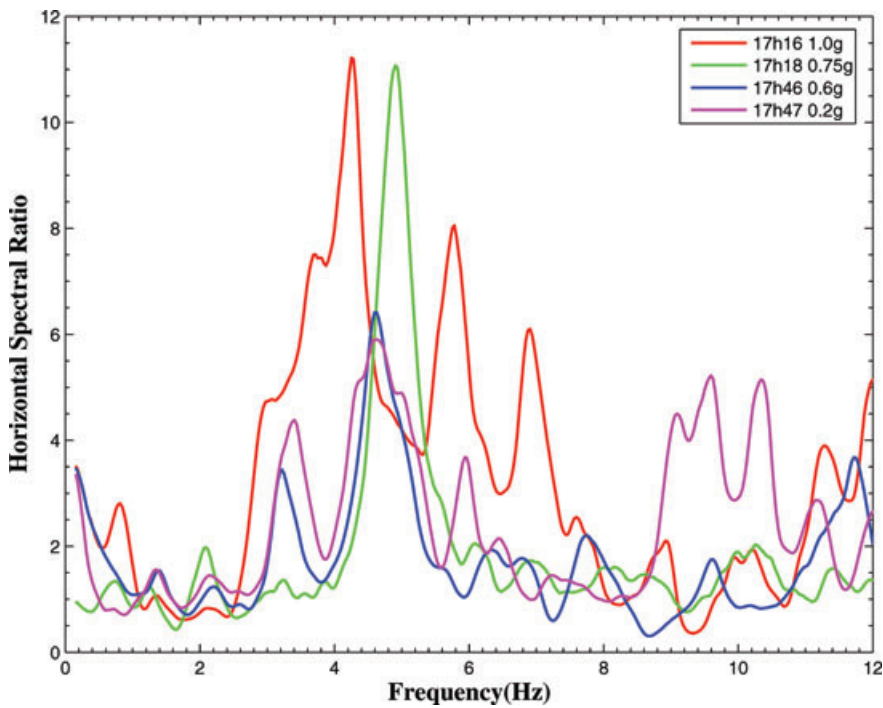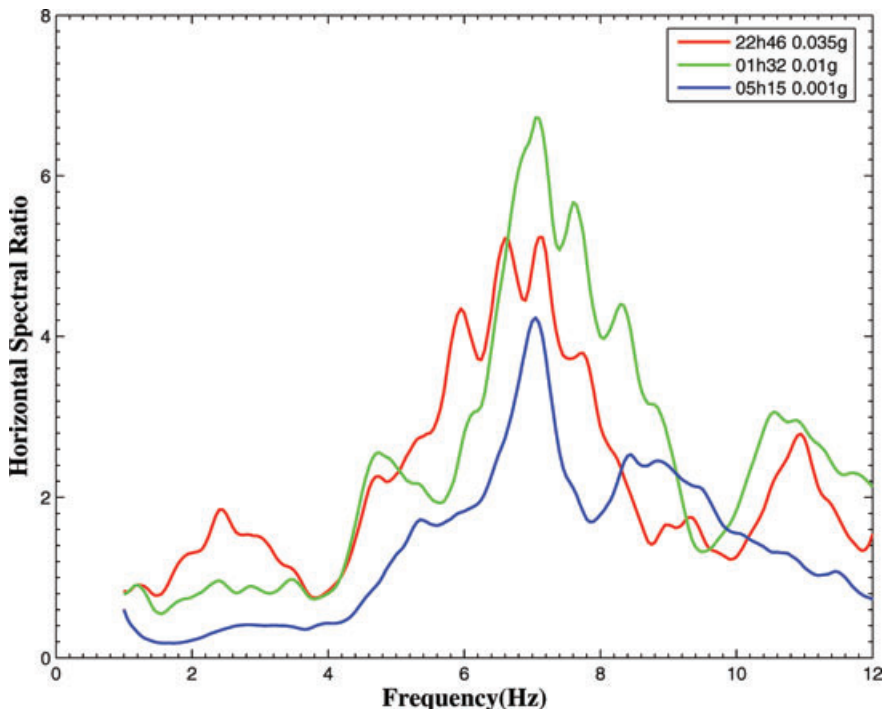
Figure 9. Horizontal spectral ratios between the two farthest stations of the array A4 and A1 for the strongest aftershocks.

respectively. We computed Fourier spectra by applying 10 per cent cosine taper at both ends. The tests we performed on the interpolation of the peaks did not show any artificial shift on the peak frequency. For the main shock and the strongest aftershock, for which peak accelerations are about 1.0 g, the peak amplification occurs around 4 Hz. For the aftershocks with peak accelerations of 0.75, 0.6 and 0.2 g maximum amplification occurs around 5 Hz.

As shown in Fig. 10, the peak amplification for weaker-felt aftershocks (PGA < 0.05 g) consistently occurs at higher frequency

(around 6–7 Hz) and seems independent of the level of acceleration reached. Spectral ratios calculated on the background noise, displayed in Fig. 11, have the same shape as the ones of the weaker-felt aftershocks.

Fig. 12 compares the amplification/frequency curves for the whole range of peak ground accelerations. The frequency shift of the peak amplification with increasing peak acceleration between 6 and 7 Hz for noise and weak motion to around 4 Hz at 1 g—is clearly observed. This shift is indicative of the non-linear response of the

Figure 10. Horizontal spectral ratios between the two farthest stations of the array A4 and A1 for three small aftershocks.
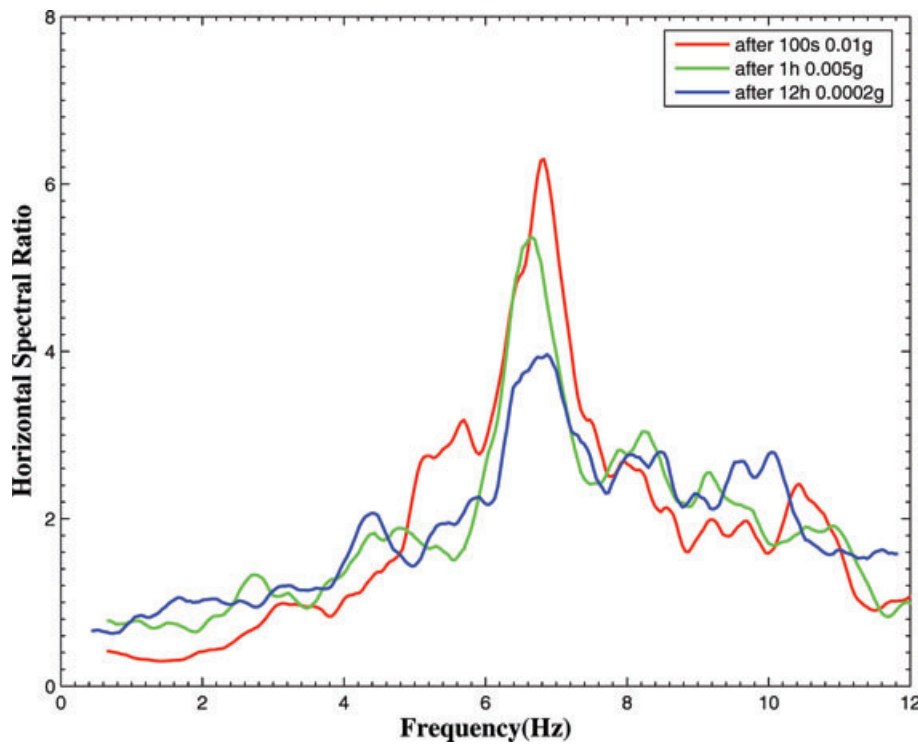
Figure 11. Horizontal spectral ratios between the two farthest stations of the array A4 and A1 for three noise windows following the main shock.
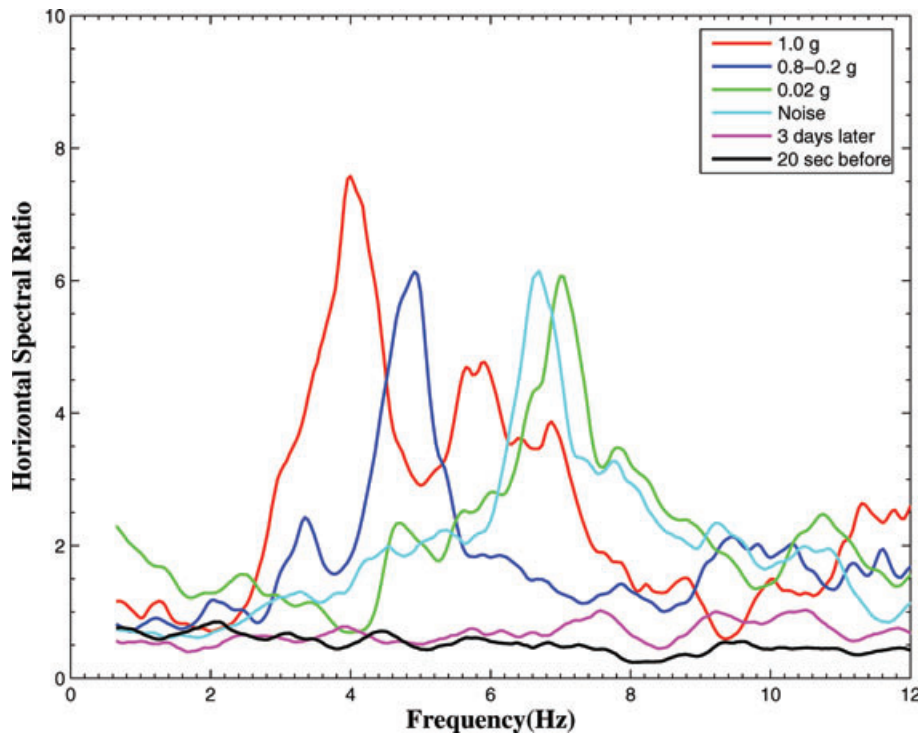
Figure 12. Average horizontal spectral ratios between the two farthest stations of the array A4 and A1 for the strong, weak motion and noise.

fault zone to seismic excitation. By analogy with the non-linearity commonly observed in soils, a likely explanation for this shift is the reduction in shear modulus of the medium when it undergoes large strains. Another observation on Fig. 12 is that the spectral ratios of the background noise 20 s before and 3 d after the main shock shows no amplification.

The spectral ratios of the background seismic shaking measured over three 1-min time windows 100 s, 1 h and 12 h after the earthquake (Fig. 11) have similar shapes with their spectral peak between 6 and 7 Hz, thus suggesting that 'linear elastic' fault zone properties are soon recovered once episodes of strong ground shaking are over. This seems confirmed in Fig. 13 by the time–frequency plots
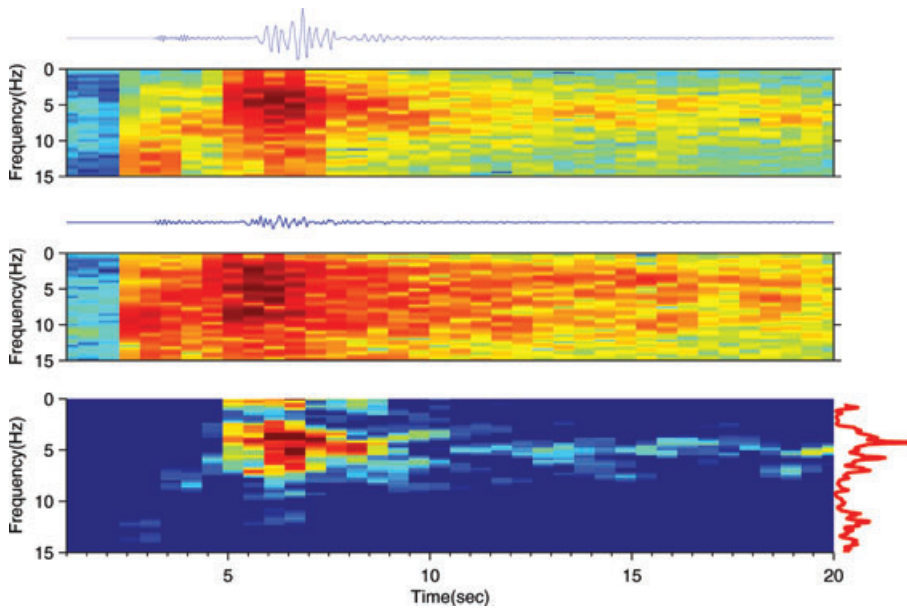
Figure 13. Time–frequency analysis of the aftershock at 17 h 16 recorded at station A4 with 1.0 g peak acceleration (top), A1 with 0.21 g peak acceleration (middle) and the relative amplifications (A4/A1) between the two stations (bottom). The spectral ratio of two stations is on the right of the bottom figure.

of the ground motion at stations A1 and A4 for the aftershock with 1.0 g peak acceleration. While outside the fault zone (A1) spectral amplitude is rather uniformly spread over the range from 1 to 10 Hz, in the middle of the fault zone (A4) most of the ground shaking occurs over a narrower frequency band which is centred around 4 Hz during the strong shaking and around 6–7 Hz a few seconds after the strong shaking has stopped. The time–frequency plot of the spectral ratio between the two sites shows the progressive shift of the amplification peak towards its higher frequency weak-motion position as the intensity of ground shaking diminishes.

## PROPOSED MECHANISM FOR FAULT ZONE BEHAVIOUR

Several factors can cause the amplification of ground motion in the fault zone, for example, elastic properties and geometry of the fault zone, shallow soil structure, source directivity, radiation pattern and path effects. The factors related to the source and path effects can be ignored since the events have similar distances, azimuths and source mechanisms (Fig. 1). Although patches of sediments are present in the area, the recording sites are surrounded by numerous limestone outcrops. The presence of hard rock at the surface throughout the area seems to eliminate the most often encountered mechanism of amplification/non-linearity which is associated with the presence of unconsolidated sediments (e.g. Beresnev & Wen 1996; Pavlenko & Irikura 2002).

In order to shed some light on the mechanism responsible for the observed fault zone behaviour, we first try to estimate the changes in the elastic parameters of the fault zone implied by the observations from spectral ratios. For this, we relate the shifts in the peak frequencies to the reductions in shear wave velocities. Reduction in shear wave velocity and increase in damping beyond a certain level of deformation are well established in geotechnical engineering. The fundamental resonance frequency f of a low velocity layer of thickness H sandwiched between two half-spaces is proportional to the wave velocity $f = V/2H$. Thus the reduced velocity with increased strain will shift the resonance to lower frequencies.

The width of the fault zone in the region studied and its shear wave velocity in the low-strain regime have been obtained by Ben-Zion *et al.* (2003) from the study of guided waves in the fault zone. They are, respectively, about 100 m and 1500 ms^{-1}. Shear wave velocity of surrounding rocks is about 3200 ms^{-1}. Quality factors inside and outside the fault zone were estimated at 10 and 1000, respectively (Ben-Zion *et al.* 2003).

We use these parameters and the 2-D analytical solution of Ben-Zion (1989) and Ben-Zion & Aki (1990) to compute the ground motion inside and outside the fault zone. The method does not account for 3-D variations and only the plane-parallel layered FZ model is considered. However, this is not a severe limitation since the geometry causing FZ related effects is mostly 2-D. The source is a shear dislocation located at a depth of 3 km slightly off the fault zone. Two receivers are located at the surface: one in the middle of the fault zone and the other 150 m away from it. The first calculation is done using the low-strain fault-zone velocity and quality factor estimated by Ben-Zion *et al.* (2003): 1500 ms^{-1} and 10. In subsequent calculations the velocity is reduced first to 1000 ms^{-1} and then to 800 ms^{-1} with quality factors of 6 and 4, respectively. The spectral amplitude ratios between the ground motion computed at these two sites are shown in Fig. 14. The peak amplifications takes place at 7, 5 and 4 Hz for the velocities of 1500, 1000 and 800 ms^{-1}, respectively. These amplifications closely correspond to the observed spectral peaks for PGA <0.1, 0.2–0.6 and 1.0 g, respectively (Fig. 12). Although the parameters of the fault zone and the source–receiver locations may not be the only combination resulting in the amplification at these frequencies, it is important to realize that a significant reduction in the velocity of the fault zone is necessary to fit the observed peak amplifications at the three intensity levels of ground motion.

If the resonance frequency of the fault zone is dependent on the level of input motion, this also implies non-linearity between stress and strain. Since we have an array with receivers closely spaced we can calculate the stress and strain from the two closest receivers (A3 and A4). The components of distance between A3 and A4 parallel and orthoganal to the fault are 280 and 20 m, respectively (Table 1). We obtain the displacement time histories U at the two
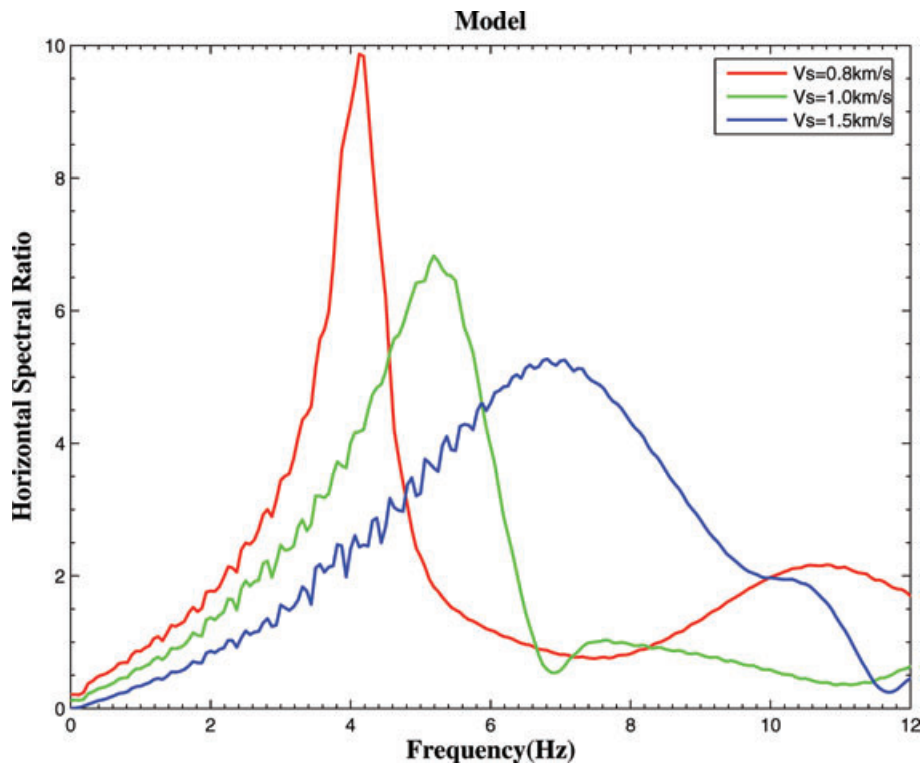
Figure 14. Ratios of the velocity spectra between two receivers 150 m apart for three fault-zone shear wave velocities.
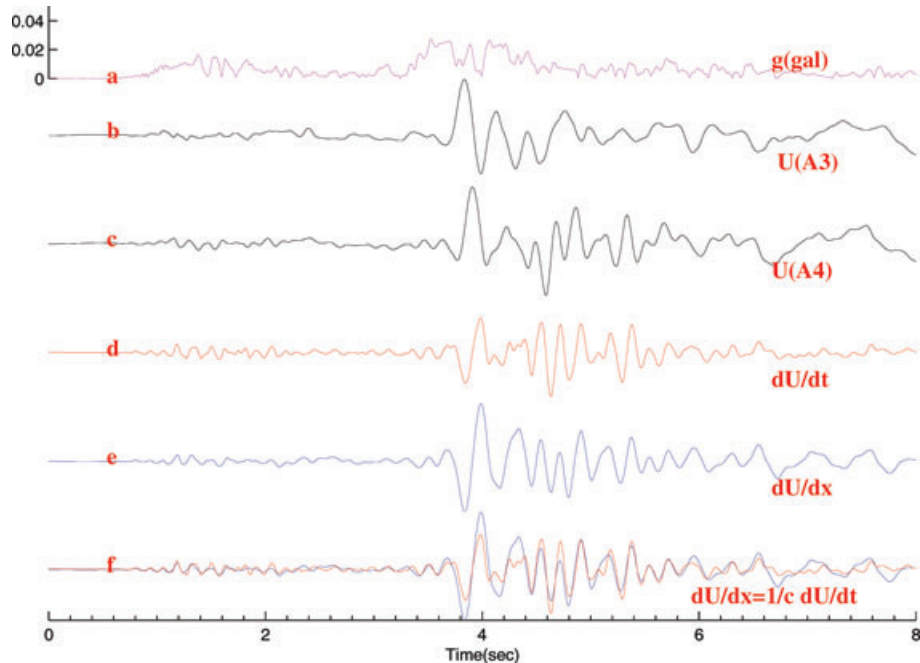
Figure 15. Change in strain during the aftershock at 17 h 13 with a peak acceleration of 0.04 g. The envelope of the acceleration recorded at station A4 (a), the displacements calculated from the accelerations at stations A3 (b) and A4 (c), the particle velocity calculated at A4 (d), the estimated dU/dx from the displacements A3 and A4 (e) and the correlation between the strain and particle velocity scaled with fault zone velocity (f).

receivers and compare strain ($dU/dx = $ [U(A4)–U(A3)]/dx) and stress ($dU(A4)/cdt$). The velocity would be equal to velocity of the fault zone for plane waves travelling horizontally. However, we expect that the apparent velocity is higher than the true medium velocity since plane *SH* waves in the fault zone are propagating non-horizontally. The velocity will only affect the amplitude of the

strain. Therefore, we can choose the appropriate velocity for weak motion case which will match the amplitudes of the stress and strain. The same velocity is then used during the computation of the strain in strong shaking. We compute stress and strain for two aftershocks with peak acceleration of 0.04 and 1.0 g, respectively. Fig. 15 shows the analysis for the aftershock with PGA of 0.04 g. Although some
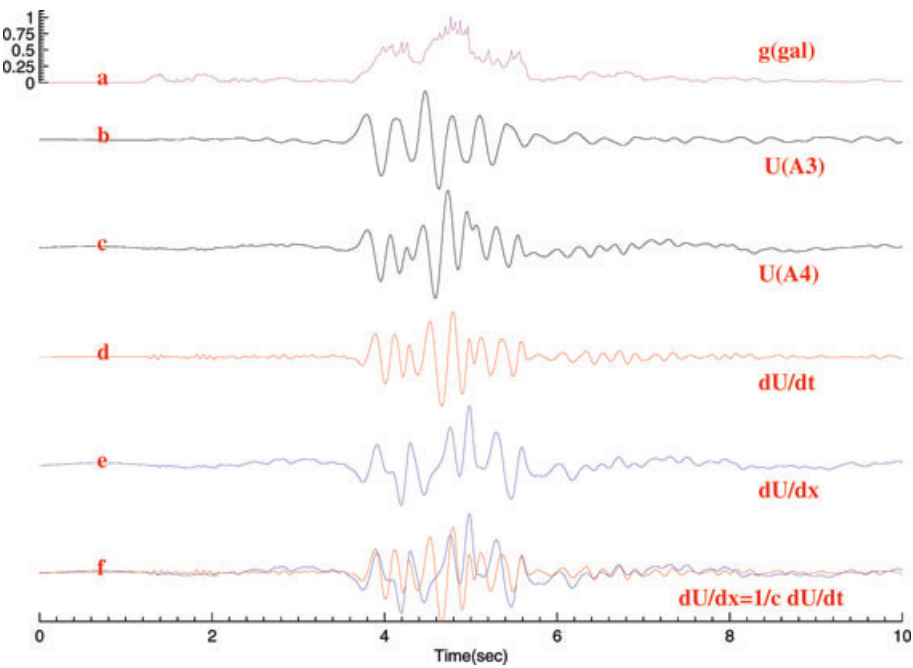
Figure 16. Change in strain during the aftershock at 17 h 16 with a peak acceleration of 1.0 g. The envelope of the acceleration recorded at station A4 (a), the displacements calculated from the accelerations at stations A3 (b) and A4 (c), the particle velocity calculated at A4 (d), the estimated dU/dx from the displacements A3 and A4 (e) and the correlation between the strain and particle velocity scaled with fault zone velocity (f).

differences exist between amplitudes both stress and strain are in phase which is an indication of linearity. However, the second aftershock with peak acceleration of 1.0 g has a different behaviour (Fig. 16). The stress and strain are in phase at the beginning but become out of phase when the acceleration level increases, which seems consistent with a temporary change in the elastic properties of the fault zone rocks induced by the strong shaking. A few seconds later the stress and strain are in phase again, suggesting, as also observed in Fig. 13, that the original elastic properties of the fault zone are recovered only a few seconds after the strong shaking is over.

It is well known that the elastic properties of crustal rocks evolve when the stress–strain conditions are beyond those associated with the linear elastic regime (e.g. Jaeger & Cook 1979). Among several factors, the presence of dry or fluid-filled cracks is probably the most important source for changes in the elastic properties of rocks in the fault zone. The changes in shear wave velocity can be related to the presence of cracks using the theory of equivalent homogenous media (Hudson 1981). An alternative view on the degradation of elastic moduli and strength of the material as a result of an increase in crack density is proposed by Hamiel *et al.* (2004), who developed a viscoelastic damage model for stable and unstable fracturing.

However, Hudson's theory of equivalent medium is simple and has been successfully applied to fractured media (e.g. Kelner *et al.* 1999). This theory states that a fractured material containing cracks randomly distributed in position has the same elastic response as an equivalent homogeneous material provided that the excitation wavelengths are large compared to the size of the cracks and the concentration of the cracks is not too large. For dry cracks parallel to each other, the shear wave speed c of the equivalent medium is, to the first order in (νa^3), given by the relation (Hudson 1981)

$$c^2 = \beta^2[1 - (16/3)(\nu a^3)[(\lambda + 2\mu)/(\lambda + \mu)\cos 2\theta \sin 2\theta$$
$$+ (\lambda + 2\mu)/(3\lambda + 4\mu)(\cos 2\theta - \sin 2\theta)^2],$$

where ν the number density of cracks per unit volume, a is the mean radius of the cracks, λ, μ, α and β denote, respectively, the two Lamé coefficients and the P- and S-wave velocities of the solid unfractured material and θ is the angle between the direction of propagation and the normals to the cracks.

The corresponding quality factor is given by

$$Q^{-1} = (\nu a^3)(\omega a/\beta)^3 1/15\pi[(3/2 + \beta^5/\alpha^5)$$
$$\times \{16/3(\lambda + 2\mu)/(3\lambda + 4\mu)\}^2 \cos^2 2\theta$$
$$+ (2 + 15/4\beta/\alpha - 10\beta^3/\alpha^3 + 8\beta^5/\alpha^5)$$
$$\times \{4/3(\lambda + 2\mu)/(\lambda + \mu)\}^2 \sin^2 2\theta].$$

Our choice of dry cracks rather than fluid-filled ones is based on the rapid change and recovery of elastic properties of the fault zone which seems to preclude any fluid flow mechanism. The choice of cracks aligned rather than randomly oriented is derived from the anisotropy study of Peng & Ben-Zion (2004) which shows the existence along this fault segment of a fast polarization direction parallel to the fault strike, similar to observations made near other strike-slip faults (Bouin *et al.* 2000), suggesting the presence of fault-parallel cracks.

Using in these expressions $\beta = 1500$ ms^{-1}, $\lambda = \mu$ and $\theta = 45°$ (the cracks are assumed to be parallel to the fault plane and the incoming shear waves to be refracted in the fault zone from their outside travel path), and setting the frequency at 7 Hz, which is the value at which peak amplification occurs in the linear elasticity domain, we estimate the crack density and size which are needed to reduce the shear wave velocity in the fault zone. We find that a reduction of shear wave speed from 1500 to 1000 ms^{-1} with a corresponding Q value of 8 would be achieved by the presence or the opening, throughout the 100 m wide fault zone, of about 400 cracks of about 50 m radius per km^2 of fault. A crack density 25 per cent higher, that is about 500 cracks per km^2 of fault, would reduce the velocity to 800 ms^{-1}. These values are just meant as

rough estimates and they are certainly outside the strict domain of validity of the expressions above.

DISCUSSIONS

Classical non-linearity observed in soils is characterized by a reduction in seismic wave velocities and an increase in damping with larger strains. In the fault zone, we do not observe de-amplification of the waves, that is a reduction in ground motion, as would be expected if the same mechanism was at work. Our observations and modelling suggest that non-linearity in the fault zone is caused by a different physical mechanism: the opening of pre-existing cracks throughout the fault zone. Although a portion of the seismic energy is dissipated during the opening of cracks, the significant reduction of the seismic velocity creates larger impedance with the surrounding high velocity structures resulting in larger amplifications. The observation that elastic fault zone properties are soon recovered following episodes of large strains shows that cracks and fissures close rapidly after the strong shaking is over.

One outcome of this study suggests that FZ are highly fractured media. Although this result in itself is not novel and not surprising, the observation that cracks in this zone seem highly sensitive to seismic shaking is somewhat new and unexpected. If the proposed mechanism to explain the observed fault zone non-linear behaviour is correct, namely the opening of numerous cracks during strong shaking, it must have other implications as well. In view of the magnitude of the non-linear effects observed here, it seems likely that non-linearity may occur locally in the fault zone under much smaller strains. If this high-sensitivity of near-surface fault-zone cracks to earth shaking is also true at seismogenic depth, the crack-opening proposed mechanism might play a role in the triggering of earthquakes by seismic waves.

Although the observations from the array was interpreted in terms of the non-linearity in the fault zone we should not rule out complex wave propagation effects. The array was installed in an area with rugged topography and complex geology. Therefore, wave propagation effects such as interference of multiple arrivals, topography and 3-D effects may create complexities and modulate spectra. Some of the simplifying assumptions such as a planar fault zone may not be satisfactory. However, we do not have detailed geological and geotechnical data to test some of the hypotheses.

CONCLUSIONS

Recordings of the ground accelerations at a small array close to the fault during the Düzce earthquake and its aftershocks show the strong spatial variability of peak acceleration over distances of only a few hundred metres. During the main shock, we recorded values ranging from 0.3 to about 1.0 g at stations distant by 1.5 km only. For one aftershock, peak acceleration values of 0.21, 0.33, 0.68 and about 1.0 g were obtained at the four stations of the array, spanning a total distance range of 1.5 km. The spatial variations on the peak acceleration is a result of the fault zone related site effects. The observed shifts on the peak frequencies with increasing peak accelerations is associated with the non-linear ground motion within the fault zone during the passage of high dynamic strain waves. As much as 45 per cent reduction in the shear wave velocity of the fault zone with a thickness of 100 m is necessary to explain observed anomalies. The near-instantaneous recovery of the fault zone indicates that the state of material did not change, that is, there was no creation of new cracks but just a change in the configuration.

REFERENCES

Akyuz, H.S., Hartleb, R., Barka, A., Altunel, E., Sunal, G., Meyer, B. & Armijo, R., 2002. Surface rupture and slip distribution of the 12 November 1999 Duzce earthquake (M 7.1), North Anatolian Fault, Bolu, Turkey, *Bull. Seism. Soc. Am.,* **92,** 61–66.

Ben-Zion, Y., 1989. The response of two joined quarter spaces to SH line sources located at the material discontinuity interface, *Geophys. J. Int.,* **98,** 213–222.

Ben-Zion, Y., 1998. Properties of seismic fault zone waves and their utility for imaging low velocity structures, *J. geophys. Res.,* **103,** 12 567–12 585, 6549–6568.

Ben-Zion, Y. & Aki, K., 1990. Seismic radiation from an SH line source in a laterally heterogeneous planar fault zone, *Bull. seism. Soc. Am.,* **70,** 971–994.

Ben-Zion, Y. *et al.*, 2003. A shallow fault zone structure illuminated by trapped waves in the Karadere-Düzce branch of the north Anatolian fault, western Turkey, *Geophys. J. Int.,* **152,** 699–717.

Beresnev, A.I. & Wen, K.-L., 1996. Nonlinear soil response—a reality ?, *Bull. seism. Soc. Am.,* **86,** 1964–1978.

Bouchon, M. & Karabulut, H., 2002. A note on seismic activity near the eastern termination of the Izmit rupture in the hours preceding the Düzce earthquake, *Bull. seism. Soc. Am.,* **92,** 406–410.

Bouin, M.P., Cocco, M., Cultrera, G., Sekiguchi, H. & Irikura, K., 2000. The rupture process of the Mj = 7.2 1995 Hyogo-ken Nanbu (Kobe) earthquake deduced from *S*-wave polarization analysis, *Geophys. J. Int.,* **143,** 521–544.

Bouin, M.P., Bouchon, M., Karabulut, H. & Aktar, M., 2004. Rupture process of the 1999 November 12 Duzce (Turkey) earthquake deduced from strong motion and GPS measurements, *Geophys. J. Int.,* **159,** 207–211.

Cormier, V.F. & Spudich, P., 1984. Amplification of ground motion and waveform complexities in fault zones: examples from the San Andreas and the Calaveras faults, *Geophys. J. R. astr. Soc.,* **79,** 135–152.

Dodge, D.A. & Beroza, G.C., 1997. Source array analysis of coda waves near the 1987 Loma Prieta, California, mainshock: implications for the mechanism of coseismic velocity changes, *J. geophys. Res.,* **102,** 24 437–24 458.

Field, H.E., Johnson, A.P., Beresnev, A.I. & Zeng, Y., 1998. Nonlinear groun- motion amplification by sediments during the 1994 Northridge earthquake, *Nature* **390,** 599–602.

Fohrmann, M., Jahnke, G., Igel, H. & Ben-Zion, Y., 2001. Guided waves generated by sources outside a low velocity fault zone layer, *EOS, Trans. Am. geophys. Un.,* **82,** F886.

Fohrmann, M., Jahnke, G., Igel, H. & Ben-Zion, Y., 2004. Guided waves from sources outside faults: an indication for shallow fault zone structure?, *Pure appl. Geophys.,* **161,** 2125–2137.

Hamiel, Y., Liu, Y., Lyakhovsky, V., Ben-Zion, Y. & Lockner, D., 2004. A visco-elastic damage model with applications to stable and unstable fracturing, *Geophys. J. Int.,* **159,** 1155–1165.

Herece, E. & Akay, E., 2003. 1:100.000 geological maps of the North Anatolian Fault, Appendix 3 and 4, Gen. Dir. of Miner. Res. and Explor., Ankara.

Hudson, J.A., 1981. Wave speeds and attenuation of elastic waves in material containing cracks, *Geohys. J. R. astr. Soc.,* **64,** 133–150.

Igel, H., Ben-Zion, Y. & Leary, P., 1997. Simulation of *SH* and *P–SV* wave propagation in fault zones, *Geophys. J. Int.,* **128,** 533–546.

Igel, H., Jahnke, G. & Ben-Zion, Y., 2002. Numerical simulation of faultzone guided waves: accuracy and 3-D effects, *Pure appl. Geophys.,* **159,** 2067–2083.

Jaeger, J.C. & Cook, N.G.W., 1979. *Fundamentals of rock mechanics,* 3rd edn., Chapman and Hall, London.

Jahnke, G., Igel, H. & Ben-Zion, Y., 2002. 3-D calculations of fault zone guided wave in various irregular structures, *Geophys. J. Int.,* **151,** 416–426.

Karabulut, H., Özalaybey, S., Taymaz, T., Aktar, M., Selvi, O. & Kocaoğlu, A., 2003. a tomographic image of the shallow crustal structure in the Eastern Marmara, *Geophys. Res. Lett.,* **30,** 2277–2280.

Kelner, S., Bouchon, M. & Coutant, O., 1999. Characterization of fractures in shallow granite from the modeling of the anisotropy and attenuation of seismic waves, *Bull. seism. Soc. Am.,* **89,** 706–717.

Leary, P.C., Li, Y.G. & Aki, K., 1987. Observations and modeling of fault zone fracture anisotropy, I, P, SV, SH travel times, *Geophys. J. R. astr. Soc.,* **91,** 461–484.

Li, Y.G., Aki, K., Adams, D., Hasemi, A. & Lee, W.H.K., 1994. Seismic guided waves trapped in the fault zone of the Landers, California earthquake of 1992, *J. geophys. Res.,* **99,** 11 705–11 722.

Li, Y.G., Vidale, J.E., Aki, K., Xu, F. & Burdette, T., 1998. Evidence of shallow fault zone strengthening after the 1992 M7.2 Landers, California, Earthquake, *Science,* **279,** 217–219.

Li, Y.G., Vidale, J.E., Aki, K. & Xu, F., 2000. Depth-dependent structure of the landers fault zone from trapped waves generated by aftershocks, *J. geophys. Res.,* **105,** 6237–6254

McGuire, J. & Ben-Zion, Y., 2005. High-resolution imaging of the Bear Valley section of the San Andreas fault at seismogenic depths with fault-zone head waves and relocated seismicity, *Geophys. J. Int.,* **162,** 1–12

Özalaybey, S., Aktar, M., Ergin, M., Karabulut, H., Bouchon, M., Tapirdamaz, C. & Yoruk, A., 2000. Aftershock studies following recent earthquakes in Turkey, paper presented at XXVII General Assembly, *Eur. Seismol. Comm.*, Lisbon Univ., Lisbon, Portugal.

Pavlenko, O. & Irikura, K., 2002. Changes in shear moduli of liquefied and nonliquefied soils during the 1995 Kobe earthquake and its aftershocks at three vertical array sites, *Bull. seism. Soc. Am.,* **92,** 1952–1969.

Peng, Z., Ben-Zion, Y., Michael, A.J. & Zhu, L., 2003. Quantitative analysis of seismic trapped waves in the rupture zone of the 1992 Landers, California earthquake: Evidence for a shallow trapping structure, *Geophys. J. Int.,* **155,** 1021–1041.

Peng, Z. & Ben-Zion, Y., 2004. Systematic analysis of crustal anisotropy along the Karadere-Düzce branch of the north Anatolian fault, *Geophys. J. Int.,* **159,** 253–274.

Peng, Z. & Ben-Zion, Y., 2005. Spatio-temporal variations of crustal anisotropy from similar events in aftershocks of the 1999 M7.4 Izmit and M7.1 Düzce,Turkey, earthquake sequences, *Geophys. J. Int.,* **160,** 1027–1043.

Peng, Z. & Ben-Zion, Y., 2006. Temporal changes of shallow seismic velocity around the Karadere-Düzcebranch of the north Anatolian fault and strong ground motion, *Pure appl. Geophys.,* **163,** 567–600.

Rovelli, A., Caserta, A., Marra, F. & Ruggiero, V., 2002. Can seismic waves be trapped inside an inactive fault zone ? The case study of Nocera Umbra, central Italy, *Bull. seism. Soc. Am.,* **92,** 2217–2232.

Rubinstein, J.L. & Beroza, G.C., 2004. Evidence for widespread strong ground motion in the Mw 6.9 Loma Prieta eartquake, *Bull. seism. Soc. Am.,* **94,** 1595–1608.

TenCate, J.A., Smith, E. & Guver, R.A., 2000. Universal slow dynamics in granular solids, *Phys. Rev. Lett.,* **85,** 1020–1023.

Vidale, J.E. & Li, Y.-G., 2003. Damage to the shallow Landers fault from the nearby Hector Mine earthquake, *Nature,* **421,** 524–526.

APPENDIX A

An example is presented to illustrate the interpolation of the clipped signal. The input signal in Fig. A1 is an aftershock of the Düzce earthquake. The signal was normalized to 1 g and then clipped at 0.75 g. Cubic spline interpolation was used to recover the clipped part of the signal. The Fig. A1 also shows the per cent error between input signal and interpolated signal.
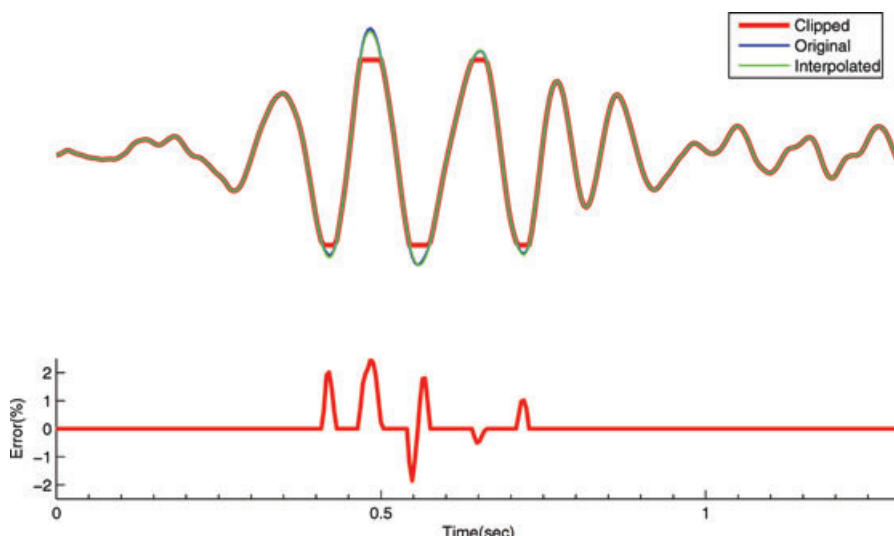
Figure A1. Test of the interpolation scheme used to recover clipped acceleration recordings. (a) Clipped seismograms at 75 per cent of maximum amplitude (red) interpolated (green) and original (blue) and (b) per cent error between original and interpolated recordings.